

The effect of progressively increasing lithium coatings on plasma discharge characteristics, transport, edge profiles and ELM stability in the National Spherical Torus Experiment

This article has been downloaded from IOPscience. Please scroll down to see the full text article.

2012 Nucl. Fusion 52 083001

(<http://iopscience.iop.org/0029-5515/52/8/083001>)

View [the table of contents for this issue](#), or go to the [journal homepage](#) for more

Download details:

IP Address: 198.35.15.210

The article was downloaded on 14/06/2012 at 18:43

Please note that [terms and conditions apply](#).

# The effect of progressively increasing lithium coatings on plasma discharge characteristics, transport, edge profiles and ELM stability in the National Spherical Torus Experiment

R. Maingi<sup>1</sup>, D.P. Boyle<sup>2,3</sup>, J.M. Canik<sup>1</sup>, S.M. Kaye<sup>2</sup>,  
C.H. Skinner<sup>2</sup>, J.P. Allain<sup>4</sup>, M.G. Bell<sup>2</sup>, R.E. Bell<sup>2</sup>, S.P. Gerhardt<sup>2</sup>,  
T.K. Gray<sup>1</sup>, M.A. Jaworski<sup>2</sup>, R. Kaita<sup>2</sup>, H.W. Kugel<sup>2</sup>,  
B.P. LeBlanc<sup>2</sup>, J. Manickam<sup>2</sup>, D.K. Mansfield<sup>2</sup>, J.E. Menard<sup>2</sup>,  
T.H. Osborne<sup>5</sup>, R. Raman<sup>6</sup>, A.L. Roquemore<sup>2</sup>, S.A. Sabbagh<sup>7</sup>,  
P.B. Snyder<sup>5</sup> and V.A. Soukhanovskii<sup>8</sup>

<sup>1</sup> Oak Ridge National Laboratory, Oak Ridge, TN 37831, USA

<sup>2</sup> Princeton Plasma Physics Laboratory, PO Box 451, Princeton, NJ 08543, USA

<sup>3</sup> Princeton University, 1 Nassau Hall, Princeton, NJ 08544, USA

<sup>4</sup> Purdue University, 400 Central Drive, West Lafayette, IN 47907, USA

<sup>5</sup> General Atomics, 3550 General Atomics Ct., San Diego, CA 92121, USA

<sup>6</sup> University of Washington, 1410 NE Campus Parkway, Seattle, WA 98195, USA

<sup>7</sup> Columbia University, 1130 Amsterdam Avenue, New York, NY 10027, USA

<sup>8</sup> Lawrence Livermore National Laboratory, 7000 East Avenue, Livermore, CA 94550, USA

Received 14 November 2011, accepted for publication 9 May 2012

Published 13 June 2012

Online at [stacks.iop.org/NF/52/083001](http://stacks.iop.org/NF/52/083001)

## Abstract

Lithium wall coatings have been shown to reduce recycling, suppress edge-localized modes (ELMs), and improve energy confinement in the National Spherical Torus Experiment (NSTX). Here we document the effect of gradually increasing lithium wall coatings on the discharge characteristics, with the reference ELMy discharges obtained in boronized, i.e. non-lithiated conditions. We observed a *continuous* but not quite monotonic reduction in recycling and improvement in energy confinement, a gradual alteration of edge plasma profiles, and slowly increasing periods of ELM quiescence. The measured edge plasma profiles during the lithium-coating scan were simulated with the SOLPS code, which quantified the reduction in divertor recycling coefficient from  $\sim 98\%$  to  $\sim 90\%$ . The reduction in recycling and fuelling, coupled with a drop in the edge particle transport rate, reduced the average edge density profile gradient, and shifted it radially inwards from the separatrix location. In contrast, the edge electron temperature ( $T_e$ ) profile was unaffected in the H-mode pedestal steep gradient region within the last 5% of normalized poloidal flux,  $\psi_N$ ; however, the  $T_e$  gradient became steeper at the top of the H-mode pedestal for  $0.8 < \psi_N < 0.94$  with lithium coatings. The peak pressure gradients were comparable during ELMy and ELM-free phases, but were shifted away from the separatrix in the ELM-free discharges, which is stabilizing to the current-driven instabilities thought to be responsible for ELMs in NSTX.

(Some figures may appear in colour only in the online journal)

## 1. Introduction

Rapidly growing instabilities known as edge-localized modes (ELMs) are commonly observed in high-confinement (H-mode) regimes in many toroidal confinement devices. The reduction or elimination [1] of ELMs while maintaining high

energy confinement is essential for ITER, which has been designed for H-mode operation. Detailed analysis has shown that large ELMs are triggered by exceeding either edge current density limits (kink/peeling modes) and/or edge pressure gradient limits (ballooning modes) [2–4]. Similar edge stability calculations using model equilibria have indicated

that spherical tokamaks should have access to higher pressure gradients and H-mode pedestal heights than higher aspect ratio tokamaks, owing to high magnetic shear and possible access to second stability regimes [5]. Nevertheless spherical tokamaks have observed a wide variety of ELM types, many in common with higher aspect ratio tokamaks [6, 7]; true ELM-free regimes with high pedestal pressure gradients have been rare. Over the last few years, however, the use of lithium evaporation onto the plasma-facing components (PFCs) of the National Spherical Torus Experiment (NSTX) [8] has enabled access to a high pedestal pressure regime, one in which the core stability limits with high normalized pressure are observed with no sign of ELMs [9].

Lithium wall coatings have been used in a variety of devices to control edge recycling and improve energy confinement [10–14]. Lithium was first introduced into NSTX in 2005 via pellet injection, with modest, short-lived effects on the discharge characteristics [15]. A lithium evaporator (LiTER) was installed in 2007 to coat the lower portion of NSTX, resulting in reduced recycling, improved energy confinement, and an elimination of ELMs [16]. In 2008, a second LiTER was installed into NSTX to provide 360° coverage of the lower divertor, thereby eliminating shadowed regions [17, 18]. Lithium from the previous campaign's experiments had been removed by sanding of the tiles during the vent prior to the operations. Approximately a month of dedicated experiments using periodic boronization of the graphite PFCs was used to provide reproducible ELMy H-modes with good energy confinement. The lithium was then introduced gradually but systematically, to thoroughly document its impact on global discharge characteristics, including ELM activity and changes to plasma profiles. The amount of lithium deposition between discharges was chosen carefully such that the transition from ELMy to ELM-free discharges would occur over at least ten discharges. Note that this experiment entailed lithium evaporation on the graphite PFCs, as was executed before the recent installation of the 'liquid lithium divertor' [19].

Limited portions of the analysis of this discharge sequence is published elsewhere [9, 20–22], including a high-level summary [23] of the findings from this paper. The role of this paper is to present additional analysis for the discharge sequence, and to tie together the previous studies to provide a more complete picture of how the application of lithium wall coatings leads to ELM suppression. The rest of this paper is organized as follows. In section 2, we provide detailed comparisons of the lithiated, ELM-free discharges and boronized, ELMy discharges, i.e. the end points of the experimental sequence. In section 3, we describe the entire discharge sequence with progressively increasing lithium wall coatings, showing how plasma parameters changed nearly *continuously* as pre-discharge lithium evaporation was increased. A strong correlation between ELM suppression and density profile broadening is documented. In section 4, we describe the interpretive 2D edge plasma simulations, including divertor recycling and the inferred change in edge transport. In section 5, we discuss laboratory experiments on plasma–material interactions (PMI) that bear on the question of how lithium pumps deuterium, including the possible role of oxygen impurities. We summarize the results in

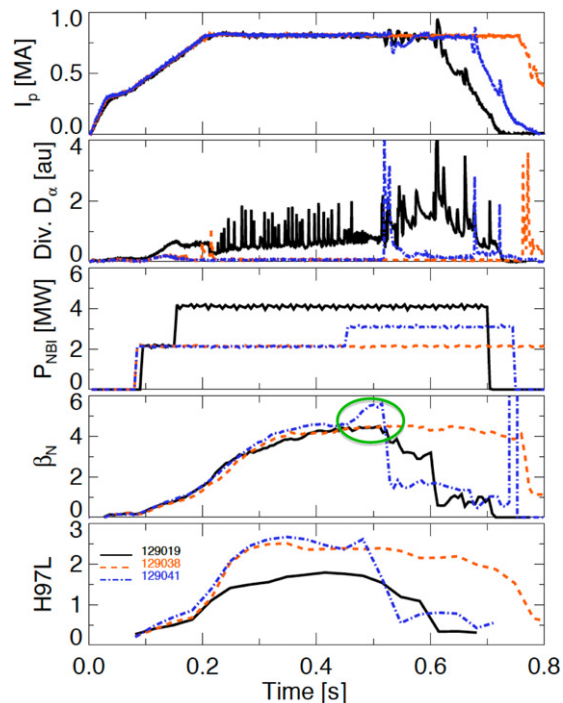


**Figure 1.** Comparison of one of the reference pre-lithium ELMy discharge (black), and two with-lithium discharges at high pre-discharge lithium evaporation with different NBI power (blue, orange): (a) plasma current  $I_p$ , (b) upper divertor  $D_\alpha$  emission, (c) NB injected power  $P_{\text{NBI}}$ , (d) normalized plasma pressure,  $\beta_N$  (e) confinement time relative to ITER97-L scaling.

section 6, schematically depicting the steps by which lithium wall coatings lead to ELM suppression.

## 2. Comparison of boronized ELMy discharges and lithiated ELM-free discharges

To illustrate the dramatic effect of high lithium deposition between discharges ('high' in this context means deposition  $>400$  mg), we first compare a reference ELMy discharge with two completely ELM-free discharges. A reference scenario with ordinary type I ELMs was developed in an Alcator C-Mod/MAST/NSTX similarity experiment [24] on small ELM regimes. These ELMs had a fractional stored energy drop  $\Delta W/W \sim 2\text{--}5\%$ , nominal frequency of  $\sim 100$  Hz that increased with heating power, in a boundary shape with a relatively high X-point for NSTX, with  $\delta_r^{\text{sep}} \sim -5$  mm. Here  $\delta_r^{\text{sep}}$  is defined as the radial separation between the two separatrices (i.e. when there are two X-points) measured at the outer midplane, where the convention  $\delta_r^{\text{sep}} < 0$  means the lower X-point is closer (and hence dominant) to the plasma than the upper X-point. There were no small, type V ELMs in this discharge scenario, which are otherwise common [25] in NSTX. Other relevant discharge parameters were  $I_p = 0.8$  MA  $B_t = 0.45$  T and neutral beam (NB) injected power  $P_{\text{NBI}} = 2\text{--}4$  MW. Periodic boronizations in the run campaign had been applied prior to this experiment, and helium glow discharge cleaning (HeGDC) between discharges was employed.

Figure 1 compares the evolution of a boronized ELMy discharge (black), with two lithiated discharges, one with low input power (orange), and one with intermediate input

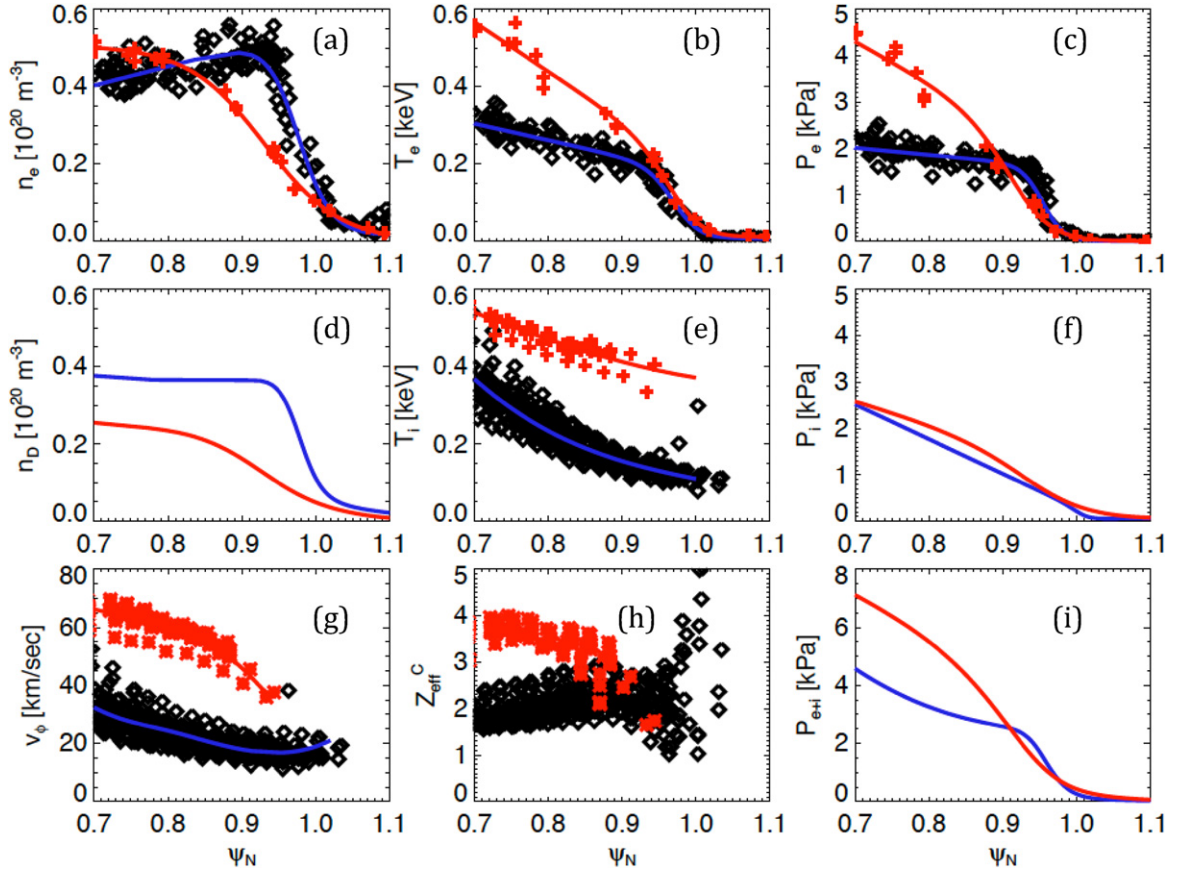


**Figure 2.** Comparison of composite profiles of reference, no-lithium (black) and lower power with-lithium discharge (red) from figure 1: (a) electron density, (b) electron temperature, (c) electron pressure, (d) deuteron density, (e) ion temperature, (f) ion pressure, (g) toroidal rotation speed, (h)  $Z_{\text{eff}}$  contribution from fully stripped carbon, and (i) total plasma pressure. Data (symbols) and profile fits (solid curves) are both shown. The reference composite profiles include data from #129015 to #129020 near 0.4 s, and the lithiated profiles fit data from #129038 near 0.55 s. The profile images were chosen at comparable line-averaged density  $\sim 4.8 \times 10^{19} \text{ m}^{-3}$ . Here  $\psi_N = (\psi - \psi_{\text{sep}})/(\psi_0 - \psi_{\text{sep}})$ , where  $\psi_{\text{sep}}$  and  $\psi$  are the poloidal flux values at the separatrix and magnetic axis, respectively.

power (blue). Panel (a) shows that the ELM-free discharges lasted longer, and panel (b) shows the ELM activity (or lack thereof) as spikes on the divertor  $D_\alpha$  emission. Note that the baseline divertor  $D_\alpha$  emission was substantially lower in the with-lithium discharges, indicating reduced recycling. At these high pre-discharge evaporation levels, the energy confinement  $\tau_E$  increased such that it was necessary to reduce  $P_{\text{NBI}}$  to avoid the global stability limit [9, 20]; hence, panel (c) shows a range in  $P_{\text{NBI}}$  from 2 to 3 MW in the discharges with lithium, compared with  $P_{\text{NBI}} = 4 \text{ MW}$  in the reference discharge. Note that many of the other discharges with high pre-discharge lithium evaporation near the end of the lithium-coating scan with  $P_{\text{NBI}} = 4 \text{ MW}$  had large locked modes shortly after the  $I_p$  flat-top (not shown). Panel (d) compares the normalized plasma pressure  $\beta_N$ , where  $\beta_N = \beta_t B_t a_m / I_p$ , and  $\beta_t = 4\mu_0 W_{\text{MHD}} / (3V_p |B_t|^2)$  is the plasma pressure normalized to the on-axis vacuum toroidal field  $B_t$ ,  $a_m$  is the minor radius,  $I_p$  is the plasma current,  $\mu_0$  is the permeability of free space, and  $W_{\text{MHD}}$  and  $V_p$  are the plasma stored energy and volume from equilibrium reconstructions. Despite the reduction in  $P_{\text{NBI}}$  from 4 to 2 MW, the orange and black discharges had a nearly identical peak  $\beta_N$  and stored energy. An additional 1 MW of  $P_{\text{NBI}}$  in the blue discharge increased  $\beta_N$  to  $\sim 5.5$ , i.e. where resistive wall modes are typically encountered [26, 27]

in NSTX. Indeed the sudden drop in  $\beta_N$  in the blue discharge at  $\sim 0.5 \text{ s}$  was concurrent with magnetohydrodynamic (MHD) activity typical of resistive wall modes. Panel (e) shows that the  $\tau_E$  normalized by the ITER-97 L-mode global scaling [28] was 50% higher in the with-lithium discharges. The discharges with lithium in figure 1 showed reduced early density and  $dN/dt$ , despite a higher gas fuelling rate [9]. The eventual density in the long-lived lowest power discharge reached the same value as the reference discharge; this was mainly due to an increase in  $Z_{\text{eff}}$  as characteristic of ELM-free H-mode. Also the radiated power fraction increased with time in these ELM-free discharges [9, 16, 18, 20], because ELMs typically flush impurities, preventing temporal accumulation. While this temporal increase in radiated power is a hindrance in developing these lithiated ELM-free discharges into long pulse scenarios, other methods have been shown to reduce impurity accumulation, e.g. with pulsed 3D fields [29, 30] or use of the ‘snowflake divertor’ configuration [31].

The modification of the plasma kinetic profiles via lithium conditioning is displayed in figure 2 for the 2 MW lithiated and 4 MW boronized discharges from figure 1. The technique used for the profile analysis is described elsewhere [32]; briefly, individual profiles are mapped to  $\psi_N$  space. These profiles are then combined in synchronization with the ELM

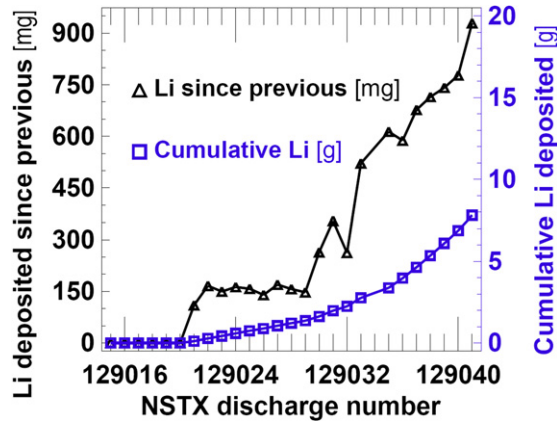


**Figure 3.** Lithium deposition during the systematic experiment: pre-discharge lithium evaporation (triangles), and cumulative lithium coating (squares).

cycle (generally using only the last 20–50% of the ELM cycle) to produce conditionally averaged composite profiles from a number of the ELM reference discharges. In the ELM-free discharge,  $\sim 100$  ms wide time windows are used to construct composite profiles; thus, profiles from multiple time bands with modest variations of  $n_e$  and collisionality can be obtained. Panel (a) shows that the electron density  $n_e$  gradient (from Thomson scattering [33, 34]) was clearly reduced in the lithiated discharge, while panel (b) shows that the electron temperature  $T_e$  gradient was comparable near the separatrix for normalized poloidal flux  $\psi_N$  from 0.95 to 1.0, but the steep gradient region extended into  $\psi_N \sim 0.8$  in the with-lithium discharge. Panel (c) shows that the edge  $P_e$  profile change largely followed the  $n_e$  profile, i.e. shifted away from the separatrix. Panel (d) shows that the lithiated discharge showed a substantial drop in the deuterium density  $n_D$ , while panel (e) shows that ion temperature  $T_i$  (from charge exchange recombination spectroscopy—ChERS [35]) was markedly higher. The changes in the  $n_D$  and  $T_i$  profiles with lithium largely offset each other, resulting in similar ion pressure ( $P_i$ ) profiles (panel (f)). Panel (g) shows that the edge ion toroidal rotation from ChERS was higher in the lithiated discharge, despite the reduction in NB power/torque, and panel (h) shows that the lithiated discharge had substantially higher  $Z_{\text{eff}}$  from carbon, likely due to the elimination of ELMs. Panel (i) shows that the shape of the total pressure gradient was dominated by the electron pressure profile shape in both cases. The peak pressure gradient is important for edge stability; we have previously shown [9, 22] that the peak pressure gradient was actually higher in some of the ELM-free composite profiles, but was uniformly shifted inwards away from the separatrix. This inward shift of the pressure profiles with lithium resulted in a similar shift of the bootstrap current, which was stabilizing to the kink/peeling modes that are thought to be responsible for these ELMs in NSTX.

### 3. Description of experiment with increasing lithium wall coatings

Lithium was introduced systematically into the ELMy H-mode discharge scenario described in the previous section. HeGDC of 6.5 min duration was used between all of

the discharges, followed by lithium evaporation from two overhead evaporators. Note that subsequent experiments demonstrated that HeGDC is unnecessary with lithium coatings between discharges. During the plasma discharges, a shutter was used to prevent lithium evaporation into the vacuum vessel to avoid coating of the windows. Figure 3 shows the lithium deposition between discharges during the sequence, as well as the cumulative deposition. The deposition rate was kept approximately constant for the first nine discharges #129021–030, and was gradually increased in the subsequent discharges. We emphasize that this sequence was the first use of lithium in this campaign, ensuring that the reference discharges were truly pre-lithium. The gas fuelling,  $P_{\text{NBI}}$ , and boundary shape were held constant until the very end of the scan, when higher fuelling and lower  $P_{\text{NBI}}$  were needed to avoid low density MHD and resistive wall modes.

The temporal evolution of the divertor  $D_\alpha$  for each discharge in the sequence is shown in figure 4. The external gas fuelling was held constant until #129036, and then it was increased for the subsequent discharges. The  $P_{\text{NBI}}$  was held constant at 4 MW until #129033, after which it was reduced in steps to avoid the locked modes.

The effects of lithium are apparent in the second lithiated discharge #129022, in that the ELM frequency was visibly reduced. ELM-free periods of increasing duration are evident in and after #129024, but the progression to fully ELM-free operation was not monotonic. Specifically discharges that ‘failed’, e.g. #129026, which had no auxiliary heating, or discharges with particularly virulent MHD modes followed by long L-mode phases, e.g. #129028 and the end of #129031, were followed by discharges with higher ELM frequency and higher recycling. The discharges #129033 and #129035–#129037 did not achieve sustained H-mode phases, as the combination of reduced heating power and increased external fuelling was not optimized until #129038. Discharges #129039 and #129041 both disrupted at 0.35 s and 0.515 s, respectively, as a result of higher  $\beta_N$  from an increased  $P_{\text{NBI}}$  to 3 MW. In addition, #129041 had modestly higher external gas fuelling than #129038 and #129039.

The evolution of edge light emission at  $t = 0.3$  s during the scan is shown in figure 5 as a function of discharge number. Panel (a) shows that the lower divertor  $D_\alpha$  gradually decreased with increasing lithium coatings, dropping substantially at the highest lithium evaporation values. Note that following the ohmic discharge #129026, the recycling light increased back to pre-lithiumization levels, before declining slowly. The magnitude of the recycling increase depends on the precise time in the discharges: at later times, e.g. at  $t = 0.4$  s, the recycling increase following the ohmic discharge #129026 was more modest [23]. Here we chose to plot the values at an earlier time because more of the discharges with high levels of lithium evaporation survived to that time before experiencing MHD activity. The centre stack and upper divertor  $D_\alpha$  gradually decreased with increasing lithium coatings also (panels (b) and (c)), showing an even larger fractional drop than the lower divertor  $D_\alpha$ ; this is likely due to the reduction in SOL density previously documented [36]. Concurrent with the decrease in  $D_\alpha$  emission was the nearly continuous increase in  $\text{Li I}$  emission from the lower divertor region, as shown in panel (d). The  $\text{Li I}$  emission from the centre stack region increased

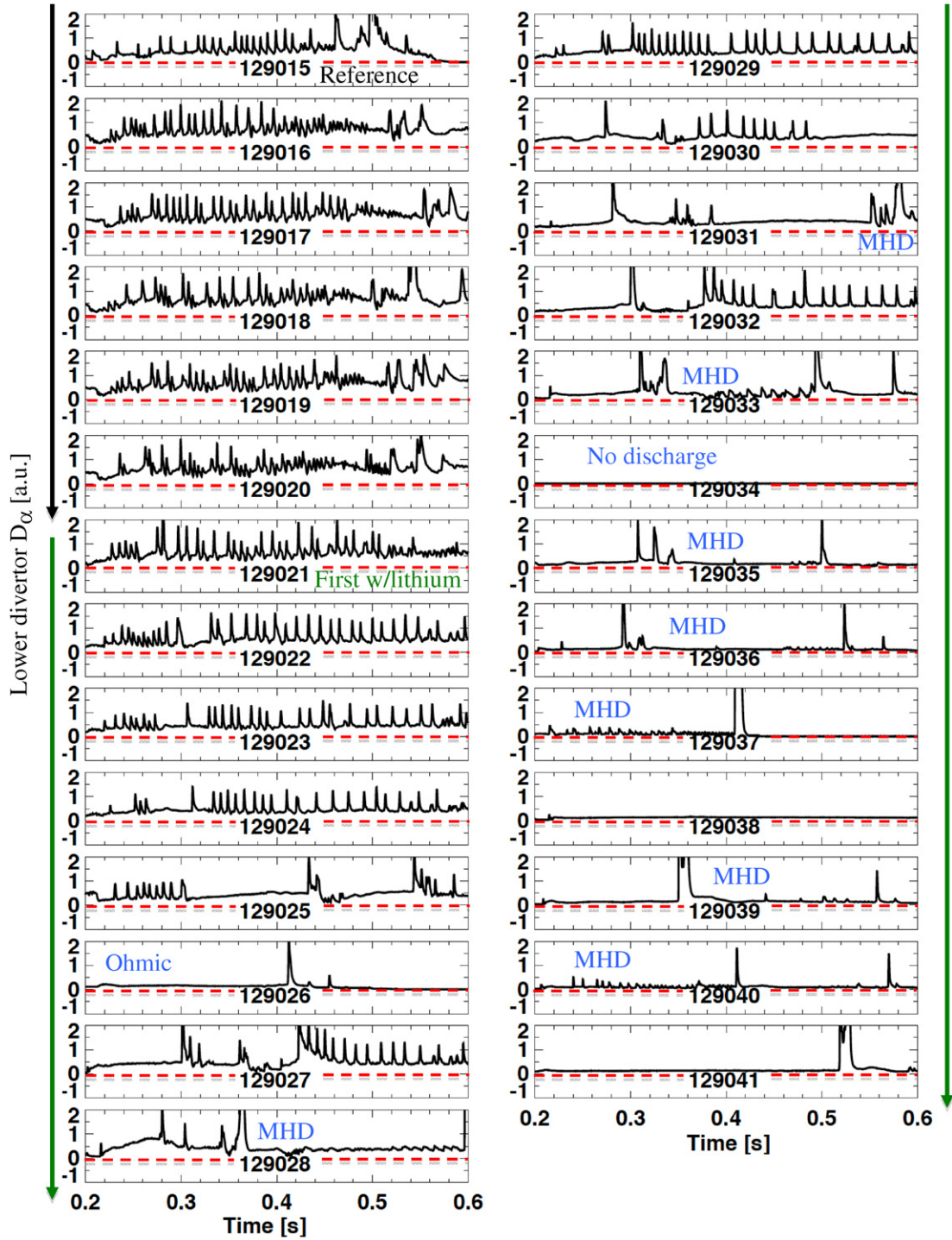


**Figure 4.** Evolution of lower divertor  $D_{\alpha}$  emission during discharge sequence, showing the gradual effect of increasing lithium evaporation on ELM activity. The black vertical arrow indicates reference, non-lithiated discharges (#129015-020), and the green arrows show lithiated discharges.

strongly with the initial lithium evaporation, but then increased more slowly with additional lithium (panel (e)). Finally the midplane neutral pressure, also sampled at  $t = 0.3$  s, decreased strongly with increasing lithium (panel (f)). These same data are plotted against the amount of pre-discharge lithium evaporation in figure 6. We note that Li-I emission from the upper divertor region did not change markedly with increasing lithium evaporation.

The evolution of other discharge parameters that are more directly plasma performance correlated, and the electron  $n_e$ ,  $T_e$ , and  $P_e$  profile peaking factors (for the discharges that lasted without significant MHD to at least 0.4 s) are correlated with the amount of pre-discharge lithium deposition, as shown in figure 7. The line-averaged density at  $t = 0.4$  s in panel (a) was gradually reduced with increasing lithium, while the peak plasma stored energy  $W_{MHD}$  and  $\beta_N$  (generally between

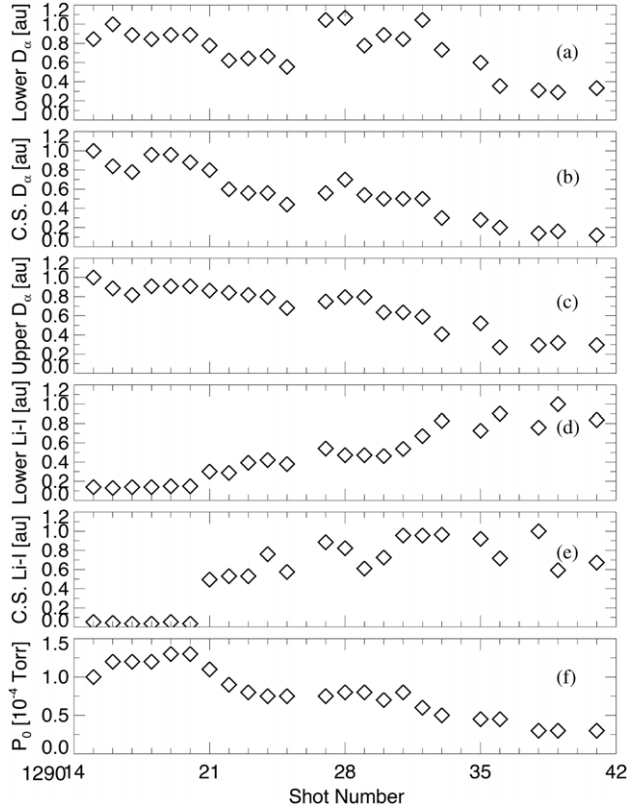


**Figure 5.** Evolution of edge light emission at  $t = 0.3$  s during the systematic lithium evaporation scan: (a) lower divertor  $D_{\alpha}$ , (b) centre stack  $D_{\alpha}$ , (c) upper divertor  $D_{\alpha}$ , (d) lower divertor Li I, (e) centre stack Li I and (f) midplane neutral pressure,  $P_0$ . For ELMy discharges, the pre-ELM baseline value is plotted. Lithium was added starting with #129021. The  $P_{\text{NBI}}$  and gas fuelling were varied in the final three discharges.

0.45 and 0.6 s) from equilibrium reconstructions gradually increased in panels (b) and (c). Panel (d) shows that the confinement enhancement factor relative to the ITER97-L scaling increased slowly during the coating scan. The  $n_e$  peaking factor (panel (e)) initially increased as the lithium deposition was increased; this is due to a general reduction in the edge density. As the discharges became less ELMy, the density profile gradient was reduced, leading to a reduced peaking factor in the latter half of the discharge sequence. On the other hand, the peaking factors of the  $T_e$  and  $P_e$  profiles in panels (f) and (g) decreased nearly monotonically with increasing lithium deposition, consistent with an analysis of a broader dataset [18]. The ion profile peaking factors did not show a clear trend during the scan.

We note that the enhancement in confinement with increasing lithium was not determined solely by the ELM frequency. Two of the three discharges with 250–350 mg lithium deposition in figure 7 were ELM-free, but the third was ELMy; nonetheless, the H-factor was comparable for all three discharges in figure 7(d). Furthermore, the H-factor increased substantially in the final three ELM-free discharges as additional lithium >400 mg was evaporated. On the other hand, the general trend of increasing H97L from 0 to 200 mg lithium deposition did correlate with the decreasing ELM frequency in those discharges.

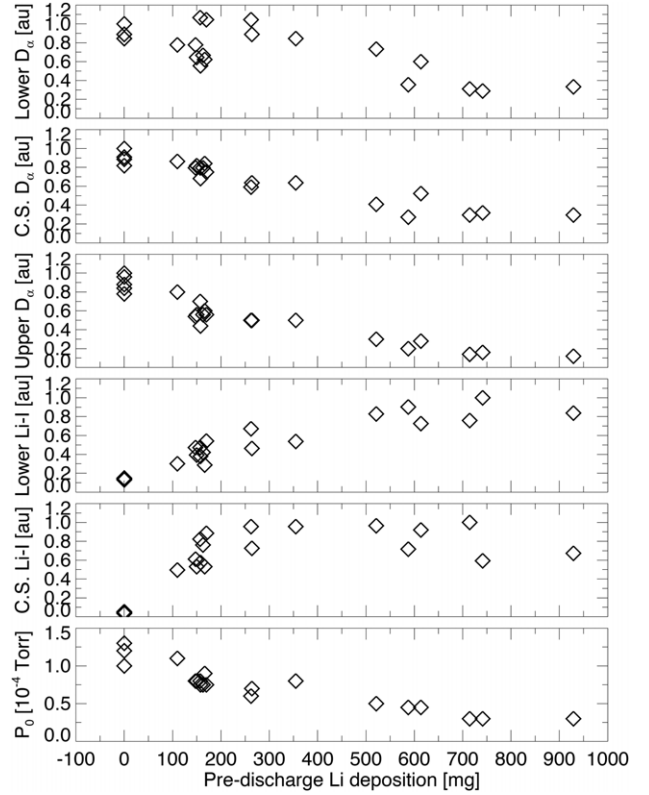


**Figure 6.** Evolution of edge light emission at  $t = 0.3$  s as a function of pre-discharge lithium evaporation: (a) lower divertor  $D_{\alpha}$ , (b) centre stack  $D_{\alpha}$ , (c) upper divertor  $D_{\alpha}$ , (d) lower divertor Li I, (e) centre stack Li I and (f) midplane neutral pressure,  $P_0$ .

The core transport during this scan was evaluated with the TRANSP code [37, 38]. The procedure uses the kinetic  $n_e$  and  $T_e$  profiles from Thomson scattering data, the  $T_i$  and  $n_C$  data from ChERS,  $Z_{\text{eff}}$  from visible Bremsstrahlung radiation, radiated power from bolometry, reconstructed equilibrium from the EFIT code [39, 40], and NB data. Monte Carlo techniques are used to compute the NB deposition, and no fast ion diffusion was used.

Figure 8 shows the results of the TRANSP analysis. Panel (a) shows that the plasma total and thermal stored energy increased with lithium deposition at constant  $P_{\text{NBI}}$ ; note that the last three discharges had reduced  $P_{\text{NBI}}$ . In general, the TRANSP calculation of stored energy was within  $\sim 10\%$  of the value from equilibrium reconstruction shown in figure 7(b); the difference in the last two discharges was larger because they were more transient. The thermal energy fraction of these discharges was typically  $\sim 75\%$ . Panel (b) shows that both the total and electron  $\tau_E$  increased with increasing lithium deposition; indeed, the electron  $\tau_E$  increased more rapidly than the global  $\tau_E$ . Panel (c) shows that the edge electron thermal diffusivity,  $\chi_e$ , at  $r/a = 0.7$  decreased strongly with increasing lithium deposition; in contrast the ion thermal diffusivity,  $\chi_i$ , actually increased modestly. The ion momentum diffusivity,  $\chi_\phi$ , was insensitive to the amount of lithium deposition, except for two of the last three discharges with the highest evaporation rate and the lowest torque input. On the other hand, the core  $\chi_e$ ,  $\chi_i$  and  $\chi_\phi$  at  $r/a = 0.35$  were insensitive to or weakly increasing with the pre-discharge lithium deposition, as shown in panel (d). These results agree with analysis [41] of a broader

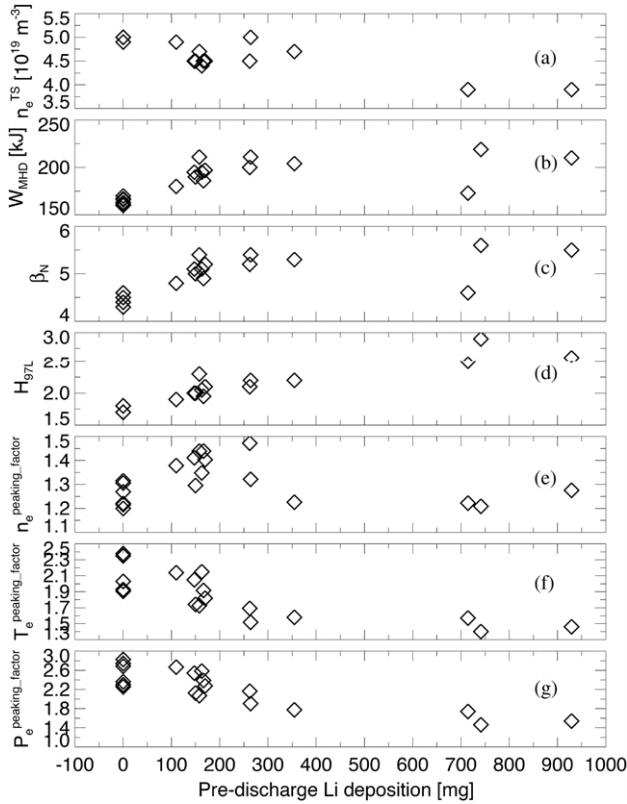


**Figure 7.** Evolution of plasma parameters and profile peaking during the systematic scan as a function of pre-discharge lithium evaporation: (a) line-averaged density from Thomson scattering ( $n_e^{TS}$ ) at  $t = 0.4$  s, (b) peak stored energy  $W_{MHD}$ , (c)  $\beta_N$  at time of peak  $W_{MHD}$ , (d) energy confinement relative to ITER97-L scaling at time of peak  $W_{MHD}$ , (e)  $n_e$  profile peaking factor, (f)  $T_e$  profile peaking factor and (g)  $P_e$  profile peaking factor. The last three discharges with highest lithium evaporation had  $PNBI = 2, 3, 3$  MW respectively.

dataset, which included a couple of the discharges from this scan. For reference, the random uncertainties for the quantities shown in figure 8 are 20–30%.

Figure 9(a) shows that the measured ELM frequency during discharges from this sequence decreased with increasing discharge number, i.e. increasing lithium deposition. As evident in figure 4, the transition to ELM-free operation was not quite monotonic; however, in that several discharges with substantial ELM-free periods were followed by ELM discharges. The data points in black in figure 9(a) had edge profiles that were analysed with the ELM-synchronization method mentioned above, whereas the data points in blue were unsuitable for profile analysis, but were included for more insight into the ELM frequency trend. There are several discharges with more than one data point per discharge in figure 9(a); in those cases, the edge profiles were analysed in non-overlapping time windows of duration  $\sim 0.1$  s. This was necessary because the discharges had both an ELM and an ELM-free phase, or long ELM-free phases with evolving density.

The  $n_e$ ,  $T_e$  and  $P_e$  composite profiles were fitted [22] with a ‘standard’ modified hyperbolic tangent (‘mtanh’) function [42], which includes both a tanh component and a linear component. The ELM frequency from the black data points is shown as a function of these pedestal widths (technically

the  $1/2$  widths, as usually quoted) in figures 9(b)–(d). The additional data points in red were obtained in discharges with heavy lithium wall coatings run in the 2009 campaign, using the same discharge programming and reduced  $PNBI < 3$  MW. The  $n_e$  and  $P_e$  profile widths in figures 9(b) and 9(d) are both shown to order the ELM and ELM-free data, mostly as a threshold criterion. The  $T_e$  profile width in figure 9(c) can be immediately ruled out as an ordering parameter. Since the lithium mainly changes the recycling and the edge fuelling, these trends support the conclusion that the density profile change is central to the ELM suppression [9, 22].

In addition to the profile widths, the profile fitting yields the pedestal top value and its location, the peak gradient and its location, and the pedestal bottom value and its location. A comprehensive analysis of the correlation between ELM frequency and the other parameters from the mtanh fits showed that ELM and ELM-free discharges were also organized by the location of the peak  $n_e$  and  $P_e$  gradients [22], i.e. the symmetry point of the tanh function. Figures 9(e)–(f) show the ELM frequency versus distance of the  $n_e$  and  $P_e$  symmetry point from the separatrix; indeed, there is a threshold distance that organizes the ELM and ELM-free data. This is unsurprising, because as the characteristic width of a profile grows, the location of its peak gradient shifts also, provided the location of the bottom of the profile remains fixed, e.g. the  $n_e$  and  $P_{e+i}$  profiles in figure 2. It is relevant, however, because the location of the symmetry point coincides with the location of the peak bootstrap and local parallel current density in the kinetic equilibria; increasing the separation between this current and the separatrix reduces the drive for kink/peeling modes. Note that the 2009 data are not included in figures 9(e)–(f) because of possible systematic uncertainty in the separatrix location for those discharges relative to the main sequence in figure 3; this uncertainty affects the computed symmetry point to separatrix distance, but not the profile widths in panels (b)–(d).

## 4. 2D interpretive modelling of the lithium wall coating scan

### 4.1. Edge transport simulations

Many of the discharges in this sequence were simulated [43] with the 2D edge plasma and neutrals code SOLPS [44] to quantify the change in edge recycling and transport. Parallel transport in SOLPS is classical, with kinetic free-streaming corrections. Recycling and other neutral source terms are computed with the Monte Carlo code, EIRENE [45]. Cross-field transport is anomalous and user-defined; in these simulations, radial profiles of the particle and thermal diffusivities were iterated to match the midplane  $n_e$ ,  $T_e$ ,  $T_i$ , and fully stripped carbon density profiles,  $n_C^{\delta+}$ . Here it was assumed that the radial transport was independent of poloidal angle; other NSTX simulations have also been carried out with poloidally dependent transport [46]. Recycling and power balance were used to match the outer divertor  $D_\alpha$  and heat flux. Thus, the final particle and thermal diffusivity profiles can be compared to interpret the effect of lithium on cross-field transport coefficients. No attempt was made to determine a particle or thermal pinch; hence,

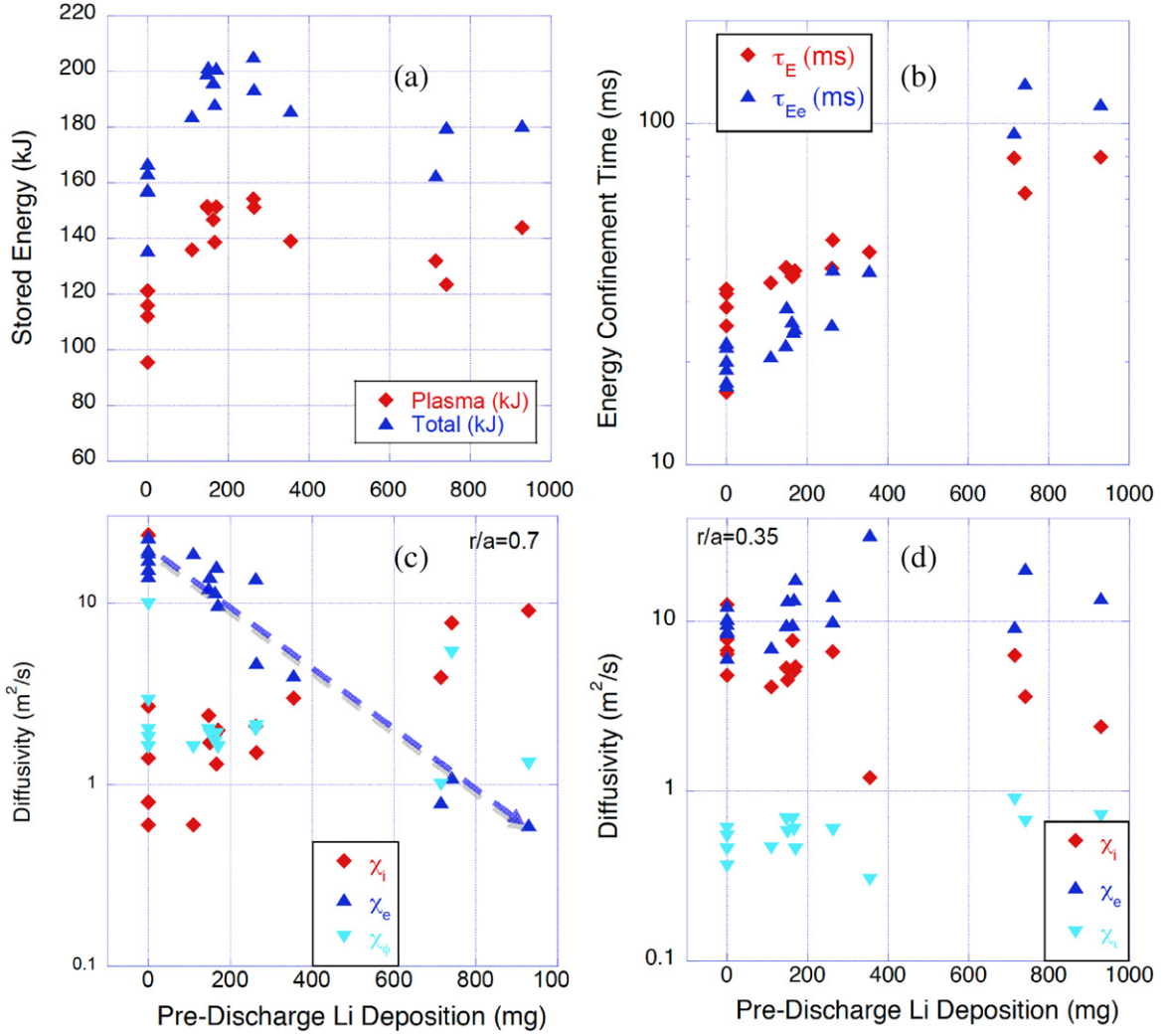


**Figure 8.** Results of core transport analysis as a function of pre-discharge lithium evaporation: (a) plasma total and thermal stored energy, (b) total and electron  $\tau_E$ , (c) cross field diffusivities  $\chi_i$ ,  $\chi_e$ , and  $\chi_\phi$  at  $r/a = 0.7$ , and (d)  $\chi_i$ ,  $\chi_e$ , and  $\chi_\phi$  at  $r/a = 0.35$ . The dashed arrow in (c) is intended to highlight the trend.

the diffusivities should be interpreted as ‘effective’ cross-field transport coefficients. The full procedure is described elsewhere [21, 43], and summarized below.

The peak value of the lower, outer divertor  $D_\alpha$  profiles measured with a 1-D CCD camera diagnostic [47] was used to constrain the divertor recycling coefficient,  $R_p$ . Figures 10(a) and (b) show the results of a  $R_p$  scan for the reference profiles from the ELMy discharges and one of the ELM-free discharges (#129038), respectively. The reference ELMy discharge peak  $D_\alpha$  emission was matched using  $R_p \sim 0.98$ , while the ELM-free peak  $D_\alpha$  emission was matched with  $R_p \sim 0.90$ . The trend is nearly identical to previous results [43] that did not model the impurities beyond a sensitivity assessment. In addition, these calculations matched the peak divertor heat flux from infrared thermography [48, 49], which effectively constrain the separatrix  $n_e$  and  $T_e$  values.

The match to the available profile data for the reference ELMy discharge #129015 is shown in figure 11, and the corresponding comparison for the ELM-free discharge is shown in figure 12. Both sets of simulations reproduce the data sufficiently well to assess the effect of lithium on the

inferred effective radial transport rates. Note that the width of the heat flux profiles in figures 11(f) and (f) is not quite right, and there is some uncertainty in the magnitude of the heat flux for the lithiated discharge, but additional simulations showed that the inferred transport rates did not critically depend on obtaining a match to the entire profile.

Figure 13 shows the results of the 2D modelling for four of the reconstructed profiles from the scan: a reference ELMy discharge based on composite ELM-synchronized plasma profiles (from #129015-019), an ELMy discharge near the transition to ELM-free operation (#129030), the subsequent ELM-free discharge (#129031), and the sustained ELM-free discharge (#129038). Panel (a) shows the match to the  $n_e$  profiles, panel (b) shows the required effective particle diffusion coefficient,  $D_e^{\text{eff}}$ , panel (c) shows the match to the  $T_e$  profiles, while panel (d) shows the corresponding effective electron thermal diffusivity,  $\chi_e^{\text{eff}}$ . The simulations show that both the  $D_e^{\text{eff}}$  and  $\chi_e^{\text{eff}}$  from the reference ELMy discharge had a minimum in the vicinity of the steep gradient region from  $0.94 < \psi_N < 1$ , indicative of the H-mode transport barrier. With increasing discharge number and lithium coatings, both

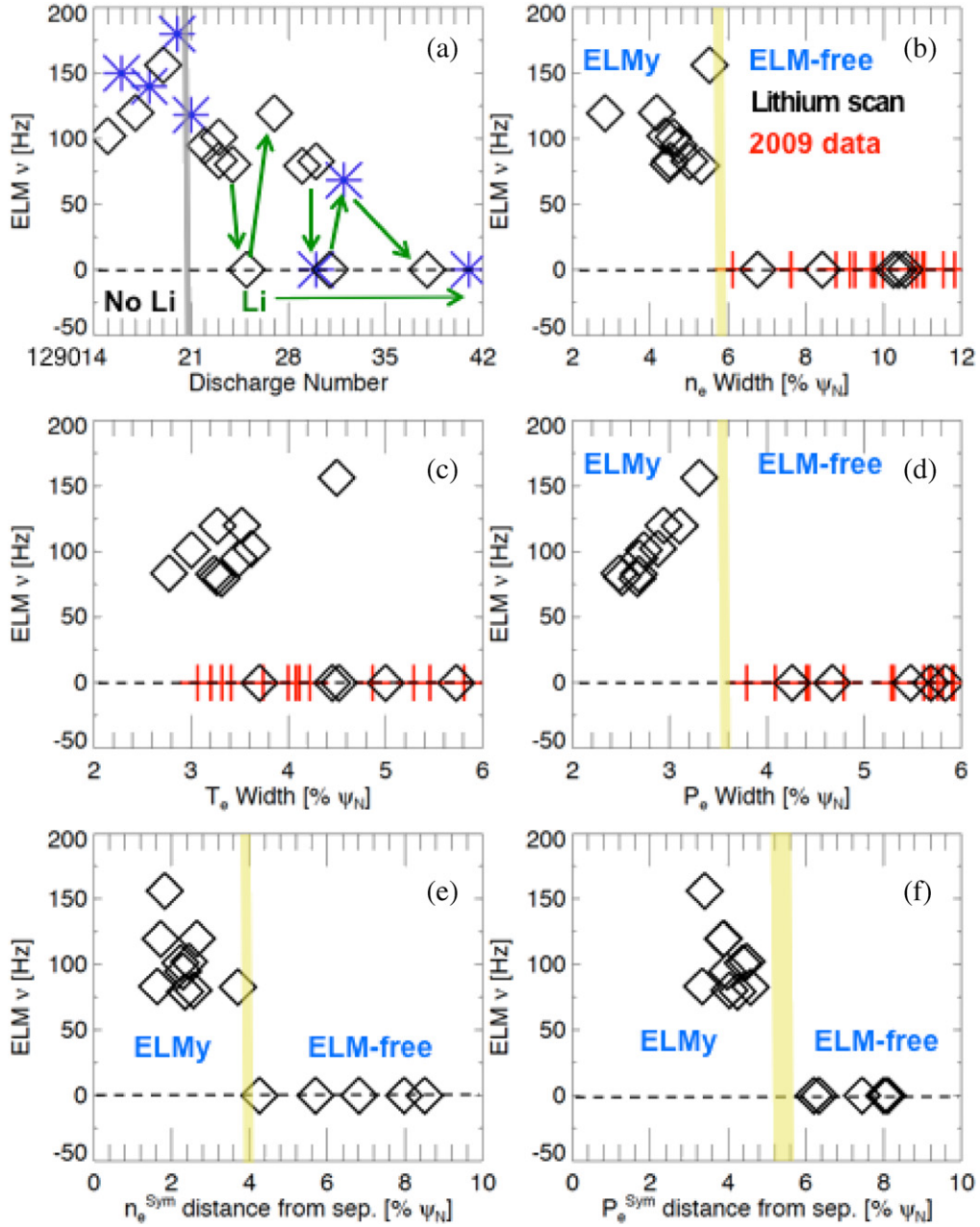


**Figure 9.** (a) Average ELM frequency during the lithium evaporation scan; discharges with both ELMy and ELM-free periods of duration  $>100$  ms are shown with multiple data points. (b) ELM frequency dependence on the fitted widths of the (b)  $n_e$ , (c)  $T_e$  and (d)  $P_e$  profiles. (e) and (f) show the ELM frequency versus the distance from the  $n_e$  and  $P_e$  tanh function symmetry points from the separatrix. Converged tanh fits could not be obtained for the blue data points in (a), but they are included to reflect the ELM frequency trend. Data from additional discharges with high pre-discharge lithium evaporation are included in red in (b), (c) and (d), but additional uncertainty in the separatrix location precludes their addition in (e) and (f).

the  $D_e^{\text{eff}}$  and  $\chi_e^{\text{eff}}$  decreased gradually in the region from  $0.8 < \psi_N < 0.94$ , until the minimum transport level extended to  $\psi_N = 0.8$ , the inner domain of the calculation. The  $D_e^{\text{eff}}$  and  $\chi_e^{\text{eff}}$  values actually increased modestly from  $0.94 < \psi_N < 1$ , and the  $D_e^{\text{eff}}$  dropped in the scrape-off layer, i.e.  $\psi_N > 1$ , for #129031 and #129038. The resilience of the  $T_e$  gradients from  $0.94 < \psi_N < 1$  in panel (c) is notable, raising the prospect of transport regulation, e.g. via electron temperature gradient (ETG) modes [21]. We emphasize that there was no prominent MHD activity, and no sign of small ELMs in these discharges.

#### 4.2. Summary of edge stability calculations

The composite fitted profiles from most of the discharges in the sequence were used to reconstruct free boundary kinetic equilibria. Perturbative variations of the edge pressure gradient and current were carried out in fixed boundary kinetic equilibria to determine the shape of the edge stability boundary with the ELITE code [3, 4]. These calculations showed [22] that the ELMy discharges were all close to the current-driven kink/peeling mode boundary within our ability to reconstruct the profiles, while the ELM-free discharges were generally

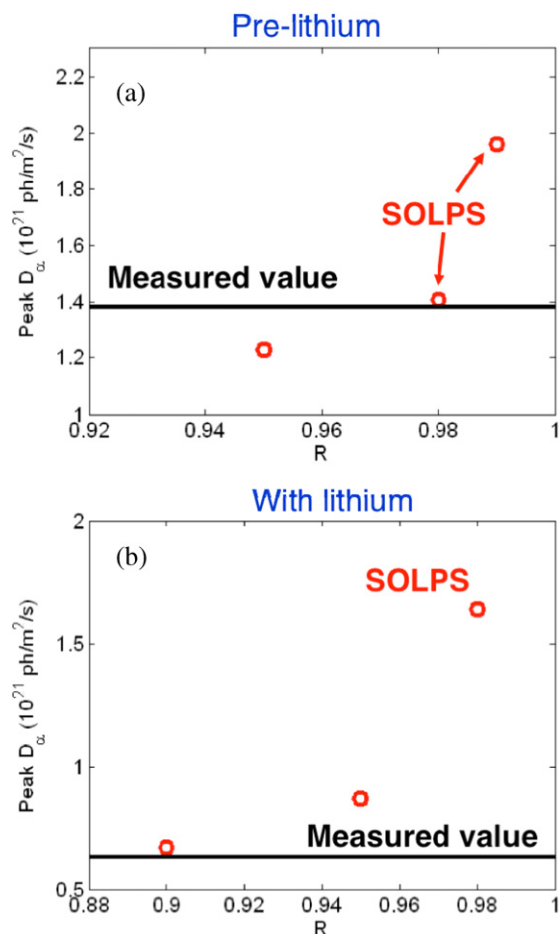


**Figure 10.** Peak divertor  $D_{\alpha}$  emission versus divertor recycling coefficient from the SOLPS calculations for (a) the pre-lithium and (b) with-lithium discharges.

farther from their kink/peeling mode stability boundaries. The reason for the enhanced stability is not simply a reduction in the peak pressure gradient; indeed, the peak pressure gradient was actually comparable in some of the ELM-free and ELMy discharge time slices [9, 22]. The primary reason for the movement of the stability boundary is that the peak pressure gradient and calculated edge bootstrap current peak were shifted inboard farther from the separatrix, which is stabilizing for the peeling mode drive. More specifically, the edge bootstrap current was reduced from  $\psi_N = 0.93$ –1, whereas it actually increased inside of that region. Note that the low aspect ratio of the NSTX naturally results in the ballooning mode part of the peeling/ballooning mode drive being small for routine boundary shapes and observed pressure profiles, although dedicated discharges with reduced lower divertor triangularity  $\sim 0.3$  began to see increase in the ballooning drive of the peeling/ballooning instabilities [50].

### 5. Possible mechanisms for lithium-based deuterium retention

The observed reduction in deuterium recycling with increasing lithium thickness on graphitic surfaces motivates an understanding of the underlying mechanism(s) responsible for the behaviour of deuterium with thin films of lithium on

graphite. In particular, the binding of deuterium to lithium coatings is influenced by lithium intercalation into graphite and therefore the observed behaviour on plasma performance is interesting since a 100% lithium coating is unattainable on graphitic surfaces. There are three independent studies that can help elucidate the underlying mechanism of continually increasing lithium-coating effects on plasma performance in NSTX.

First *in situ* PMI probe measurements [51] have identified a threshold ‘equivalent thickness’ of lithium necessary to obtain favourable hydrogen retention effects. The term ‘equivalent thickness’ is used here since lithium readily intercalates (diffuses) into the graphite bulk once deposited [52]. This is supported by the second study, which consisted of *in situ* offline laboratory data [53] where a correlation between deuterium dose and a threshold amount of lithium was established showing that about 300–500 nm of lithium is necessary to effectively impact hydrogen recycling. The calibration of about 400 mg Li deposition in the divertor region of NSTX was equivalent to about 100 nm Li thickness measured by an *in situ* PMI probe. The third and final study elucidates the behaviour of deuterium in lithiated graphite. Atomistic simulations have uncovered a new mechanism that helps explain how deuterium can bind to carbon or oxygen atoms at the surface in the vicinity of lithium [54]. Thus in addition to D–C and D–Li bonding, the D–C–Li and D–O–Li bonding channels can also exist due to the electropositive nature of Li inducing a net dipole effect on oxygen and carbon atoms thus attracting hydrogen atoms. Furthermore, it was discovered that lithiated graphite has a fluence-dependent saturation that can be as short as 1–2 s, depending on the D irradiation fluence [55]. Further work is necessary to accurately quantify this effect and correlate it back to the plasma behaviour.

### 6. Summary and conclusions

To summarize,  $D_{\alpha}$  emission from the lower and upper divertors, and centre stack was gradually reduced with increasing lithium wall coatings in NSTX; concurrently, the lower divertor Li I emission increased. Stored energy,  $\beta_N$ , and normalized energy confinement all increased, while the core  $T_e$  and  $P_e$  profiles became less peaked with increasing lithium wall coatings. Electron (ion) thermal diffusivity from TRANSP modelling was mostly unchanged at  $r/a \sim 0.35$ , but dropped (increased) continuously at  $r/a \sim 0.7$ .

The most dramatic changes to the profiles were in the H-mode pedestal region, where the  $n_e$  and  $P_e$  profile widths doubled. Interestingly, the edge  $T_e$  gradient remained approximately constant in the H-mode barrier region, but increased just inside the top of the pedestal with increasing wall coatings. The ion pressure profile was changed only modestly; hence, the total pressure profile reflected the modification of the electron pressure profile, whose peak gradient and associated bootstrap current moved farther from the separatrix. These profile changes were clearly correlated with the observed gradual suppression of ELMs with increasing lithium wall coatings, with increased margin to the kink/peeling mode window being the key stabilizing mechanism.

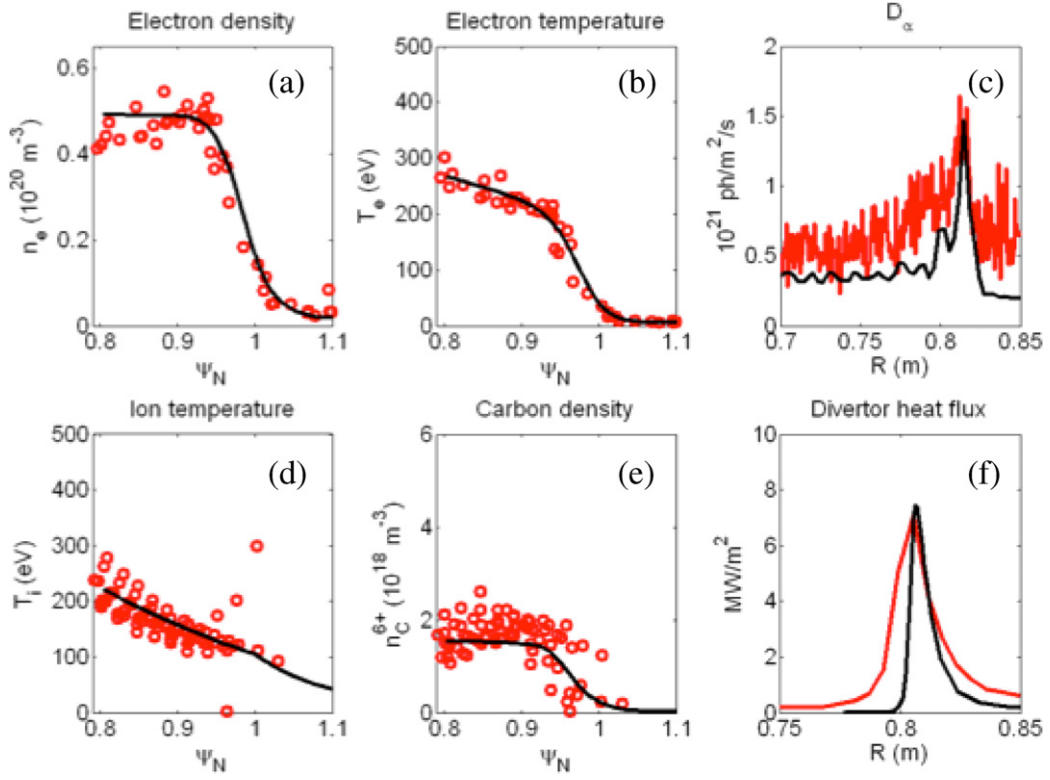


**Figure 11.** Comparison between midplane data (red) and SOLPS modelling (black) for pre-lithium ELMy discharge with  $R_p = 0.98$ : (a)  $n_e$ , (b)  $T_e$ , (c)  $T_i$ , (d)  $n_C^{6+}$ ; and divertor profile data (e)  $D_\alpha$ , and (f) heat flux.

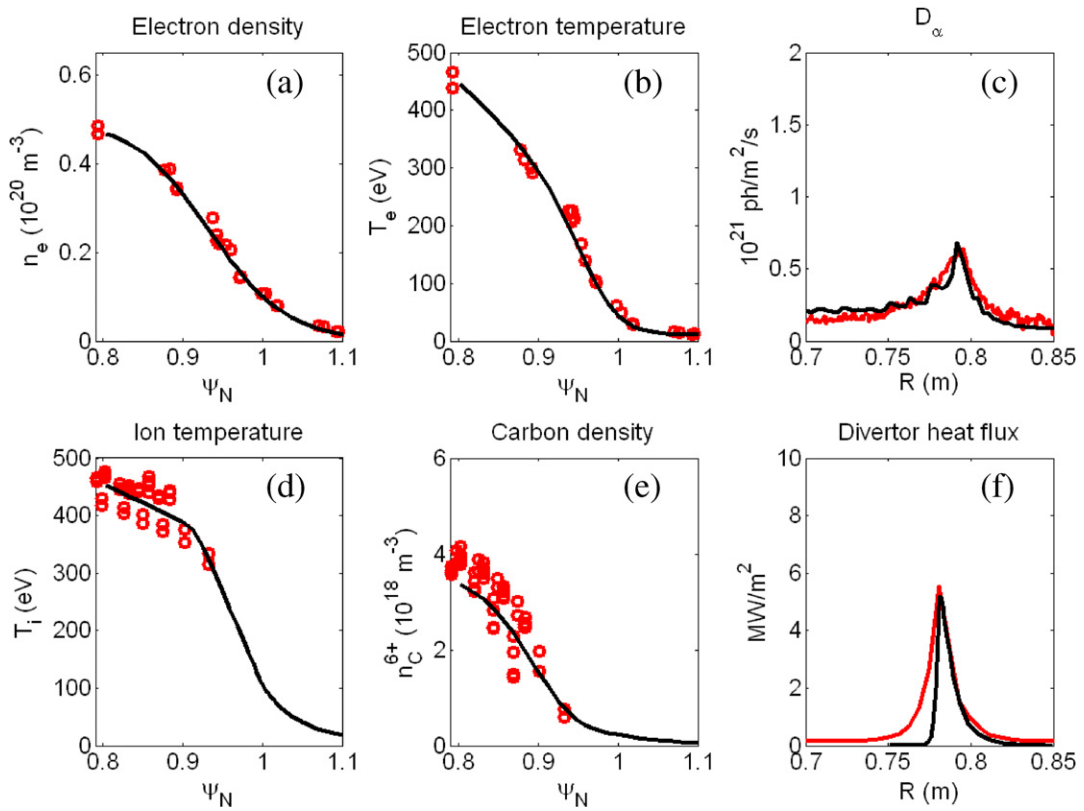


**Figure 12.** Comparison between midplane data (red) and SOLPS modelling (black) for with-lithium ELM-free discharge with  $R_p = 0.90$ : (a)  $n_e$ , (b)  $T_e$ , (c)  $T_i$ , (d)  $n_C^{6+}$ ; and divertor profile data (e)  $D_\alpha$ , and (f) heat flux.

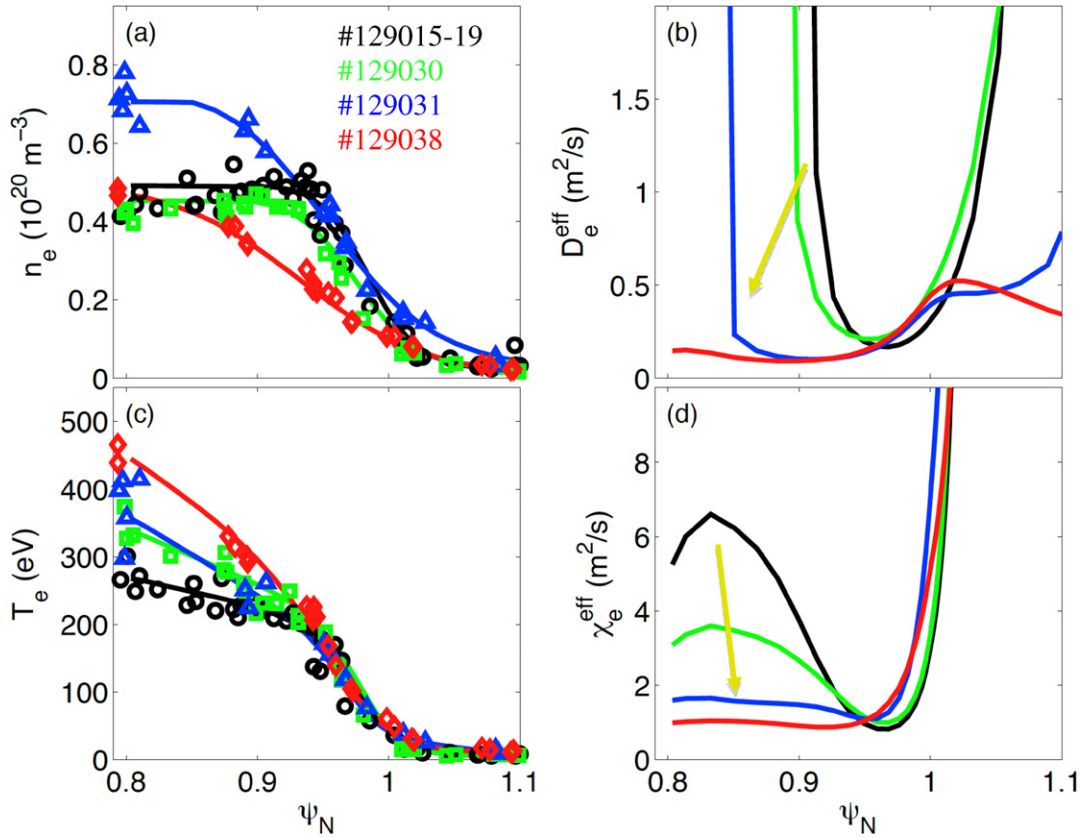


**Figure 13.** Modelling results for four discharges during the lithium deposition scan: (a)  $n_e$ , (b) effective cross-field electron diffusion coefficient  $D_e^{\text{eff}}$ , (c)  $T_e$  and (d) effective cross-field electron thermal diffusivity,  $\chi_e^{\text{eff}}$ . The yellow arrows indicate the trend with increasing lithium deposition.

Interpretive simulations with the SOLPS code showed that the edge  $D_e^{\text{eff}}$  and  $\chi_e^{\text{eff}}$  were reduced substantially from  $0.8 < \psi_N < 0.94$ , i.e. the H-mode pedestal effectively expanded to the inner boundary of the calculation in the ELM-free discharge with lithium. On the other hand, the  $D_e^{\text{eff}}$  and  $\chi_e^{\text{eff}}$  were largely unchanged from  $0.95 < \psi_N < 1$ , suggesting an instability that fixes the gradient in that region. The inferred transport reduction was largest for the highest wall coatings.

Figure 14 displays schematically the method by wall lithium wall coatings lead to ELM suppression. These steps are the following.

- (1) Lithium reduces recycling, due to its affinity for atomic hydrogenic species; the precise details of the pumping depends on complex Li-C-O-D chemistry.
- (2) The core fuelling from divertor recycling sources is reduced, reducing the edge density in the SOL and near-separatrix; concurrent with this is a drop in the edge particle and heat transport (the cause for which is under investigation).
- (3) The reduced fuelling reduces the  $n_e$  gradient; the reduced transport broadens the  $n_e$  profile width and the  $T_e$  profile width inside of  $\psi_N = 0.95$ .
- (4) The  $P_e$  follows the  $n_e$  profile; thus, the peak pressure gradient shifts away from the separatrix; because the ion pressure profile is mostly unchanged, the total pressure profile follows the electron pressure.
- (5) The edge bootstrap current profile shifts away from the separatrix, following the pressure profile; this change in

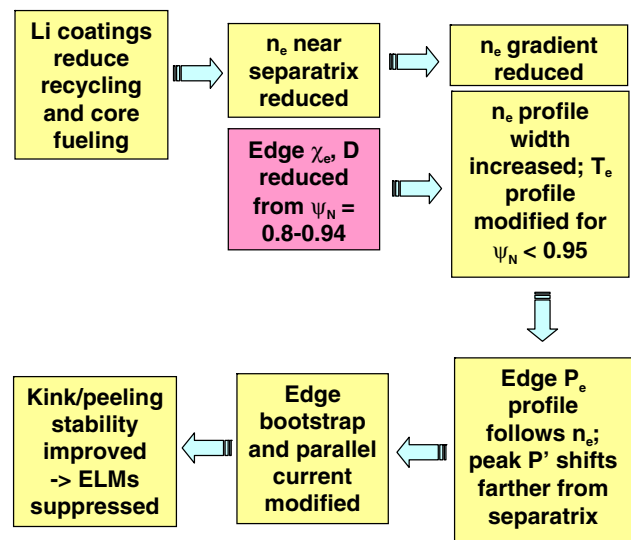


**Figure 14.** Flowchart showing how lithium coatings lead to the change of edge profiles and suppression of ELMs. The yellow boxes represent connections that are (at least) semi-quantitatively understood; the cause for the reduction in transport as displayed in the pink box is not understood.

the bootstrap current profile is reflected in the parallel current profile.

- (6) The resulting drive for the current-driven kink/peeling mode, thought to be responsible for these NSTX ELMs, is reduced.

From the observation that the progression to ELM-free discharges in figure 9(a) was not quite monotonic, we conclude that the ‘nearly continuous dependence’ in this paper does not correlate directly with the cumulative lithium deposition, which continually increased. On the other hand, the continuous dependence observed in #129021–129029 occurred at nearly constant pre-discharge lithium deposition, indicating that cumulative deposition effects cannot be ignored either. Nonetheless, the amount of pre-discharge lithium evaporation appears to be the dominant factor in determining the magnitude of the effects described in this paper. For instance ELMy discharges were converted to ELM-free discharges within 1–2 discharges with pre-discharge lithium evaporation >500 mg. Examples of these ELM-free discharges are shown by the red crosses in figures 9(b)–(d). In comparison, the first nearly ELM-free discharge in this sequence in figures 3 and 4, #129031, required a cumulative lithium evaporation of >2 g.

Present research is focused around several remaining questions. First tying all of the observed effects back to the amount of pre-discharge lithium wall coating is challenging. Even the minimum coatings result in nominal average divertor film thicknesses of 60 nm (~250 monolayers) in the vicinity of the outer strike point, with the largest evaporations approaching 500 nm thick films (~2000 monolayers). In comparison, the expected implantation depth for the NSTX divertor parameters is ~5 nm, i.e. well below the evaporative coating thicknesses [23]. We speculate that the continuous improvement in the plasma discharges is due to the achievement of some required minimum thickness in peripheral PFC regions that are otherwise modestly exposed to the lithium evaporation, e.g. the lower centre stack region. In addition, the possible important role of oxygen in the deuterium pumping in the Li–C system needs to be assessed quantitatively.

There are additional open issues regarding the edge stability. First the growth rates of the kink/peeling modes are relatively low, so that diamagnetic stabilization might be expected to stabilize them. Recent calculations with the XGC-0 code have suggested that the Sauter bootstrap current is 30–40% low at low  $R/a$  and medium to high collisionality, i.e. as was the case for the ELMy discharges in NSTX. Under these conditions the higher bootstrap current leads to higher growth rates for the kink/peeling modes. Second, it is known that the high X-point location used for these discharges leads to ordinary type I ELMs; a lower X-point leads to a mixed type V and type I ELM regime in NSTX. The effect of X-point height on edge stability calculations has not yet been analysed. Finally the effect of the uncertainty of the separatrix location on the mode growth rates is in progress; here, a two-point power balance model predicting upstream  $T_e$  of 40–70 eV was used as a constraint in the kinetic equilibrium.

Next, the mechanism for the reduction in particle and thermal transport for  $\psi_N < 0.94$ , i.e. inside the region normally thought of as the top of the H-mode pedestal, is not understood. Furthermore, the instability responsible for the clamping of the edge  $T_e$  gradient has not been conclusively identified. Without that clamping, the  $T_e$  values could have risen to maintain a constant pressure profile, which would have mostly eliminated the shift of the bootstrap current away from the separatrix.

The role of paleoclassical transport [56, 57] and ETG modes in setting the edge transport is still being assessed [21].

Specifically, the magnitude and profile of the inferred  $\chi_e^{\text{eff}}$ , as well as the overall  $n_e$  profile, agrees with that predicted by paleoclassical transport in the penultimate with-lithium discharge; direct experimental evidence for a strong particle pinch as predicted from paleoclassical transport is continuing. In addition, the increase in the  $n_e$  gradient from  $\psi_N = 0.8$ – $0.95$  with only a modest change in the  $T_e$  gradient raises the prospect of density gradient stabilization of the ETG, as observed with transient edge  $n_e$  perturbations [58]. Calculations of the microstability and resulting transport in the pedestal top region with the GS2 code are commencing.

## Acknowledgments

This research was supported in part by the US Department of Energy under contracts DE-AC05-00OR22725, DE-AC02-09CH11466, DE-FC02-04ER54698, DE-AC52-07NA27344, DE-FG03-99ER54527, DE-FG02-08ER54990 and DE-FG02-99ER54524. The authors gratefully acknowledge the contribution of the NSTX technical and operations staff.

## References

- [1] Loarte A. et al 2008 *Proc. 22nd Fusion Energy Conf. (Geneva, Switzerland, 13–18 October 2008)* IT/P6 and <http://www-naweb.iaea.org/naweb/physics/FEC/FEC2008/html/index.htm>
- [2] Connor J.W., Hastie R.J., Wilson H.R. and Miller R.L. 1998 *Phys. Plasmas* **5** 2687
- [3] Wilson H.R., Snyder P.B., Huysmans G.T.A. and Miller R.L. 2002 *Phys. Plasmas* **9** 1277
- [4] Snyder P.B. et al 2002 *Phys. Plasmas* **9** 2037
- [5] Snyder P.B., Wilson H.R., Osborne T.H. and Leonard A.W. 2004 *Plasma Phys. Control. Fusion* **46** A131
- [6] Kirk A. et al 2003 *Plasma Phys. Control. Fusion* **46** 551
- [7] Maingi R. et al 2005 *Nucl. Fusion* **45** 1066
- [8] Ono M. et al 2000 *Nucl. Fusion* **40** 557
- [9] Maingi R. et al 2009 *Phys. Rev. Lett.* **103** 075001
- [10] Snipes J., Marmor E.S. and Terry J.L. 1992 *J. Nucl. Mater.* **196–198** 686
- [11] Mansfield D.K. et al 2001 *Nucl. Fusion* **41** 1823
- [12] Majeski R. et al 2006 *Phys. Rev. Lett.* **97** 075002
- [13] Apicella M. et al 2007 *J. Nucl. Mater.* **363–365** 1346
- [14] Sánchez J. et al 2009 *J. Nucl. Mater.* **390–391** 852
- [15] Kugel H.W. et al 2007 *J. Nucl. Mater.* **363–365** 791
- [16] Kugel H.W. et al 2008 *Phys. Plasmas* **15** 056118
- [17] Kugel H.W. et al 2009 *J. Nucl. Mater.* **390–391** 1000
- [18] Bell M.G. et al 2009 *Plasma Phys. Control. Fusion* **51** 124054
- [19] Kugel H.W. et al 2009 *Fusion Eng. Des.* **84** 1125
- [20] Mansfield D.K. et al 2009 *J. Nucl. Mater.* **390–391** 764
- [21] Canik J.M. et al 2011 *Phys. Plasmas* **18** 056118
- [22] Boyle D.P. et al 2011 *Plasma Phys. Control. Fusion* **53** 105011
- [23] Maingi R. et al 2011 *Phys. Rev. Lett.* **107** 145004
- [24] Maingi R. et al 2011 *Nucl. Fusion* **51** 063036
- [25] Maingi R. et al 2005 *Nucl. Fusion* **45** 264
- [26] Menard J.E. et al 2003 *Nucl. Fusion* **43** 330
- [27] Sabbagh S.A. et al 2006 *Nucl. Fusion* **46** 635
- [28] Kaye S.M., Greenwald M. and Stroth U. 1997 *Nucl. Fusion* **37** 1303
- [29] Canik J.M. et al 2010 *Nucl. Fusion* **51** 064016
- [30] Canik J.M. et al 2010 *Phys. Rev. Lett.* **104** 045001
- [31] Soukhanovskii V.A. et al 2011 *Nucl. Fusion* **51** 012001
- [32] Osborne T.H. et al 2008 *J. Phys.: Conf. Series* **123** 012014
- [33] LeBlanc B. 2004 *Nucl. Fusion* **44** 513
- [34] LeBlanc B.P. et al 2003 *Rev. Sci. Instrum.* **74** 1659
- [35] Bell R.E. 2004 *Rev. Sci. Instrum.* **75** 4158

- [36] Kaita R. *et al* 2008 *Proc. 22nd Fusion Energy Conf. (Geneva, Switzerland, 13–18 October 2008)* paper EX/P4 and <http://www-naweb.iaea.org/napc/physics/FEC/FEC2008/html/index.htm>
- [37] Hawyrluk R.J. 1980 *Phys. Plasmas Close Thermonucl. Cond.* **1** 19
- [38] Goldston R.J. *et al* 1981 *J. Comput. Phys.* **43** 61
- [39] Lao L.L. *et al* 1985 *Nucl. Fusion* **25** 1611
- [40] Sabbagh S.A. *et al* 2001 *Nucl. Fusion* **41** 1601
- [41] Ding S. *et al* 2010 *Plasma Phys. Control. Fusion* **52** 015001
- [42] Groebner R.J. and Osborne T.H. 1998 *Phys. Plasmas* **5** 1800
- [43] Canik J.M. *et al* 2011 *J. Nucl. Mater.* **415** S409
- [44] Schneider R. 2006 *Contrib. Plasma Phys.* **46** 3
- [45] Reiter D. 1992 *J. Nucl. Mater.* **196–198** 80
- [46] Smirnov R.D. *et al* 2010 *Contrib. Plasma Phys.* **50** 299
- [47] Soukhanovskii V.A. 2004 *Rev. Sci. Instrum.* **75** 4320
- [48] Mastrovito D.M. 2003 *Rev. Sci. Instrum.* **74** 5090
- [49] Maingi R. *et al* 2007 *J. Nucl. Mater.* **363–365** 196
- [50] Sontag A.C. *et al* 2011 *Nucl. Fusion* **51** 103022
- [51] Skinner C.H. *et al* 2011 *J. Nucl. Mater.* **415** S773
- [52] Itou N., Toyoda H., Morita K. and Sugai H. 2001 *J. Nucl. Mater.* **290** 281
- [53] Taylor C.N. *et al* 2011 *J. Nucl. Mater.* **415** S777
- [54] Krstic P.S. *et al* 2011 Dynamics of deuterium retention and sputtering of Li–C–O surfaces *Fus. Eng. Des.* at press
- [55] Taylor C.N., Heim B. and Allain J.P. 2011 *J. Appl. Phys.* **109** 053306
- [56] Callen J. 2005 *Phys. Rev. Lett.* **94** 055002
- [57] Callen J.D., Hegna C.C. and Cole A.J. 2010 *Phys. Plasmas* **17** 056113
- [58] Ren Y. *et al* 2011 *Phys. Rev. Lett.* **106** 165005